Neurobiology of Disease 155 (2021) 105400

Contents lists available at ScienceDirect

Neurobiology of Disease

journal homepage: www.elsevier.com/locate/ynbdi

Disease-causing mutated ATLASTIN 3 is excluded from distal axons and reduces axonal autophagy

Laura Behrendt, Christian Hoischen, Christoph Kaether *

Leibniz-Institut für Alternsforschung-Fritz-Lipmann-Institut, 07745 Jena, Germany

ARTICLE INFO

Keywords:
Atlastin
Axonopathy
Hereditary sensory neuropathy
Endoplasmic reticulum
Autophagy

ABSTRACT

Mutations in the ER-network forming GTPase atlastin3 (ATL3) can cause axon degeneration of sensory neurons by not fully understood mechanisms. We here show that the hereditary sensory and autonomous neuropathy (HSAN)-causing ATL3 Y192C or P338R are excluded from distal axons by a barrier at the axon initial segment (AIS). This barrier is selective for mutated ATL3, but not wildtype ATL3 or unrelated ER-membrane proteins. Actin-depolymerization partially restores the transport of ATL3 Y192C into distal axons. The results point to the existence of a selective diffusion barrier in the ER membrane at the AIS, analogous to the AIS-based barriers for plasma membrane and cytosolic proteins. Functionally, the absence of ATL3 at the distal axon reduces axonal autophagy and the ER network deformation in the soma causes a reduction in axonal lysosomes. Both could contribute to axonal degeneration and eventually to HSAN.

1. Introduction

The endoplasmic reticulum (ER) forms an elaborate network of interconnected flat cisternal sheets and highly curved tubules that is distributed throughout the whole cell. The structure of the ER is regulated by different proteins that are located in the ER membrane: Climp63, p180 and Kinectin participate in sheet generation and maintenance, while Reticulons and REEPs induce membrane curvature and thereby shape ER tubules and sheet edges (for review see Chen et al., 2013; Shibata et al., 2006; Westrate et al., 2015). A critical step for network formation is the fusion of ER tubules, mediated by a class of membrane-bound GTPases known as atlastins (ATLs) (Hu et al., 2009; Orso et al., 2009).

Upon GTP binding, ATLs dimerize, which promotes membrane tethering. Subsequently, GTP hydrolysis induces conformational changes that lead to fusion of membranes and creates a new three-way-junction (3WJ). ATLs are sufficient to mediate fusion in vitro, but for efficient fusion and maintenance of 3WJs additional factors like lunapark were described (Chen et al., 2015b; Chen et al., 2012).

In addition to their role in establishing 3WJs, ATLs play a role in ER-phagy. ER-phagy is the selective autophagy of fragments of the ER (Mochida et al., 2015) mediated by specific receptors (reviewed in Chino and Mizushima, 2020; Wilkinson, 2019). ATL3 is a receptor for tubular ER-phagy (Chen et al., 2019), while all ATLs act downstream of another ER-phagy receptor, FAM134B/RETREG1 (Liang et al., 2018).

A perturbed ER morphology has detrimental effects for neurons. This is reflected by mutations in several genes coding for ER shaping proteins that cause hereditary axonopathies. Hereditary axonopathies comprise a large group of disorders affecting afferent and efferent neurons with exceptional long axons leading to the progressive loss of peripheral nerve function (Hübner and Kurth, 2014; Timmerman et al., 2013). Two heterozygous mutations in *ATL3*, resulting in amino acid changes Y192C or P338R, have been identified to cause hereditary sensory and autonomic neuropathy (HSAN)(Fischer et al., 2014; Kornak et al., 2014). Patients suffer from a loss of pain perception and destruction of the pedal skeleton. Both mutated ATL3 proteins retain their GTPase activity but are unable to cause membrane fusion, resulting in aberrant ER membrane tethering (Krols et al., 2018b). Both mutations reduce the binding to GABARAP and consequently ER-phagy (Chen et al., 2019). Functionally, ATL3 Y192C reduces ER-Golgi transport, fragments the Golgi and reduces autophagy (Behrendt et al., 2019).

The notable abundance of ER-shaping genes among all genes causing hereditary axonopathies highlight the importance of the axonal ER for neuronal homeostasis. The ER extends continuously throughout the

Abbreviations: ATL, atlastin; HSAN, hereditary sensory and autonomous neuropathy; AIS, axon initial segment; ER, endoplasmic reticulum; 3WJ, three-way-junctions; DIV, days in vitro; AnkG, ankyrinG.

* Corresponding authro at: Leibniz Institut für Alternsforschung-Fritz Lipmann Institut, Beutenbergstr. 11, 07745 Jena, Germany.
E-mail address: ckaether@fli-leibniz.de (C. Kaether).

https://doi.org/10.1016/j.nbd.2021.105400
Received 7 January 2021; Received in revised form 27 April 2021; Accepted 16 May 2021
Available online 19 May 2021

axon and forms a primarily tubular network, occasionally containing sheets (Terasaki, 2018; Wu et al., 2017; Yalcin et al., 2017). Using serial section electron microscopy, Terasaki revealed a special feature of axonal ER tubules: axonal ER tubules are narrower than ER tubules in non-neuronal cells (20–30 nm vs. 50–60 nm) (Terasaki, 2018). The reason for the different tubular diameters remains to be investigated. Imaging the narrow axonal ER using conventional light microscopy methods remains difficult, complicating the studies of mutated ER shaping proteins and their effect on axonal ER structure and function. Axonal ER functions comprise calcium storage, lipid synthesis, protein synthesis and export, among others (Luarte et al., 2018; Ozturk et al., 2020). Furthermore, the axonal ER makes extensive contact to other organelles, thereby regulating their function (Wu et al., 2017).

Recent live-cell imaging experiments have shown that the distal axonal ER is the primary site of autophagosome formation in axons (Hollenbeck, 1993; Maday and Holzbaur, 2012; Maday and Holzbaur, 2014; Maday et al., 2012a). By degrading accumulated or damaged proteins and organelles, axonal autophagy contributes to maintaining axonal homeostasis and integrity of the distal proteome (Maday, 2016). Likewise, autophagy is necessary for axonal outgrowth and regeneration (Ban et al., 2013; Fimia et al., 2007). Axonal autophagosomes mature into degradative organelles on their way to the soma by fusing to late endosomes and lysosomes (Lee et al., 2011; Maday et al., 2012a; Wang et al., 2015). After somatic entry, autophagosomes are prevented from re-entering the axon (Maday and Holzbaur, 2016).

Because of its highly specialized tasks, the protein and lipid composition of the axon is different from the soma and the dendrites. A unique structure at the proximal part of the axon, the axon initial segment (AIS), not only is the site of action potential generation but also helps to establish and maintain the structure and composition of the axon and thus neuronal polarity. The AIS consists of a dense network of cytoskeletal proteins like AnkyrinG and spectrin, ion channels in high density, fasciculated microtubules, actin and others (Huang and Rasband, 2018; Leterrier, 2018). Two mechanisms comprise the gatekeeper function of the AIS: i) a diffusion barrier at the axonal plasma membrane, segregating axonal membrane proteins from somatodendritic membrane proteins. ii) a cytoplasmic filter regulating diffusion of cytoplasmic proteins like tau and regulating vesicular transport between soma and axon (Leterrier, 2018).

We here show that HSAN-causing mutated ATL3 Y192C and P338R are excluded from distal axons by a barrier at the AIS. ATL3 Y192C expressing neurons have less axonal autophagosomes which might contribute to neurodegeneration.

2. Material and methods

2.1. Antibodies, plasmids, chemical compounds

List of antibodies

Antibody or dye	Origin,	Dilution	Supplier	RRID
anti-myc	mouse, monoclonal	1:500 (IF) 1:1000 (WB)	Santa Cruz (sc-40)	AB_627268
anti-myc	rabbit, polyclonal	1:500 (IF) 1:1000 (WB	Santa Cruz (sc-789)	AB_631274
anti-HA	mouse, monoclonal	1:500	Sigma Aldrich (H9658)	AB_260092
anti-REEP1	rabbit, polyclonal	1:500	Proteintech (17988)	AB_2178441
anti-AnkyrinG	mouse, monoclonal	1:50	Thermo Fisher (33–8800)	AB_2533145
anti-MAP2	mouse, monoclonal	1:500	Sigma-Aldrich (M4403)	AB_477193
anti-β-III-tubulin	rabbit, polyclonal	1:500	Sigma-Aldrich (T2200)	AB_262133
anti-Reticulon4	rabbit, polyclonal	1:200 (IF) 1:1000 (WB)	Abcam (ab47085)	AB_881718
anti-ATL3	rabbit, polyclonal	1:800	Abcam (ab104262)	AB_10712136
Phalloidin-Alexa Flour 568	–	1:40	Thermo Fisher (A12380)	
anti-rabbit IgG, HRP conjugate	goat	1:5000	Promega (W4011)	AB_430833
anti-mouse IgG, HRP conjugate	goat	1:5000	Promega (W4021)	AB_430834
Alexa Fluor® 555 anti-mouse	goat	1:500	Life Technologies (A-21424)	AB_141780
Alexa Fluor® 555 anti-rabbit	goat	1:500	Life Technologies (A-21429)	AB_141761
Alexa Fluor® 488 anti-mouse	goat	1:500	Life Technologies (A-11029)	AB_138404
Alexa Fluor® 488 anti-rabbit	goat	1:500	Life Technologies (A-11034)	AB_2576217
Alexa Fluor® 647 anti-rabbit	goat	1:250	Molecular Probes (A-21245)	AB_141775
Alexa Fluor® 647 anti-mouse	goat	1:250	Molecular Probes (A-21236)	AB_2535805
Alexa Fluor® 546 anti-mouse	goat	1:100	Molecular Probes (A-11030)	AB_144695

List of plasmids

Insert	Vector backbone	Source/reference	RRID
hATL3-myc	pCI	kindly provided by Ingo Kurth (Kornak et al., 2014)	
hATL3 Y192C-myc	pCI	kindly provided by Ingo Kurth (Kornak et al., 2014)	
empty	pcDNA3.1 (+)	Invitrogen (V790–20)	
GFP-hATL3	pEGFP-C1	(Behrendt et al., 2019)	
GFP-hATL3 Y192C	pEGFP-C1	(Behrendt et al., 2019)	
BFP-hATL3	pEGFP-C1	this study	
BFP-hATL3 Y192C	pEGFP-C1	this study	
mcherry-eGFP-RAMP4	pInd20	this study	
myc-hATL3 Y192C	pcDNA3.1 (+) Hygro	(Behrendt et al., 2019)	
Rtn4a-GFP	pAcGFP1-N1	kindly provided by Gia Voeltz (Shibata et al., 2008)	Addgene_61807
REEP1	pCS2 (+)	kindly provided by Christian Beetz (Beetz et al., 2012)	
RFP-LC3	FUW	kindly provided by Patrick Lüningschrör	
mcherry-DFCP1	pmCherry-1	kindly provided by Do-Hyung Kim (Kim et al., 2015)	Addgene_86746
Lamp1-RFP	Modified Clontech Plasmid	kindly provided by Walther Mothes (Sherer et al., 2003)	Addgene_1817

(continued on next column)

(continued)

(continued on next page)

(*continued*)

Insert	Vector backbone	Source/reference	RRID
ppIss-dtTomato-KDEL	pcDNA3.1 (+) Hygro	kindly provided by Christina Valkova	
GFP-Sec61b	pEGFP-C1	kindly provided by Christian Beetz,	
GFP-ATL1	pEGFP-C1	kindly provided by Justine Wagner	
GFP-ATL1 Y196C	pEGFP-C1	kindly provided by Justine Wagner	

Compound	Supplier
Dulbecco's modified Eagle medium (DMEM)	Thermo Fisher (61965059)
Minimal essential medium (MEM)	Thermo Fisher (31095029)
Neurobasal medium (NBM)	Thermo Fisher (21103049)
GlutaMAX	Thermo Fisher (35050061)
sodium pyruvate	Thermo Fisher (11360070)
HEPES	Thermo Fisher (15630106)
L-glutamine	Thermo Fisher (25030032)
HBSS	Thermo Fisher (14170088)
DNase	Sigma Aldrich (D4527)
B27 supplement	Thermo Fisher (17504044)
Cytochalasin D	Sigma Aldrich (C8273)
Latrunculin A	Sigma Aldrich (L5163)
Nocodazole	Sigma Aldrich (M1404)
Chloroquine	Sigma Aldrich (C6628)
myc-Trap agarose	Chromotek (yta-20)
GFP-Trap agarose	Chromotek (gta-20)
Novex NativePAGE 4–16% BisTris gels	Thermo Fisher (BN1002Box)
PEI	Polysciences Europe (23966–2)
Polybrene	Sigma Aldrich (107689)
sodium acrylate	SantaCruz (sc-236,893)
Methacrylic acid N-hydroxysuccinimide ester	Sigma-Aldrich (730300)
Proteinase K	AppliChem (A4392,0010)

2.2. Cloning

For construction of BFP-tagged hATL3, GFP was replaced by BFP in pEGFP-C1 GFP-hATL3. To this end, BFP was amplified from mito-BFP (Addgene 49151, kindly provided by Gia Voeltz, (Friedman et al., 2011)) using forward (fwd) primer 5'-gctagcgctaccATGAGCGAGCTGATTAAGGAGAAC-3′ introducing a *Nhe*I restriction site and reverse (rev) primer 5′- ctcgagatctgagtccggaATTAAGCTTGTGCCCCAGTTTGC-3′ introducing a *Xho*I restriction site. The restriction sites were used for cloning the fragment into pEGFP-C1 GFP-hATL3 after GFP was cut out. The Y192C mutation was introduced by standard site-directed mutagenesis. For construction of pInd20-mcherry-eGFP-RAMP4, mcherry-eGFP-RAMP4 was amplified from Tet-On mcherry-eGFP-RAMP4 (Addgene 109014, kindly provided by Jacob Corn, (Liang et al., 2018)) using fwd primer 5′- ggggacaagtttgtacaaaaaagcaggctTCGGAGAATTGGCTAGCGCC adding an attB1 site and rev primer 5′- ggggaccactttgtacaagaaagctgggtCCTACATGCCCATCCTGATACTTTG-3′ adding an attB2 site. These sites were used for cloning the insert into pDONR221 using the Gateway System. Finally, pDONR221-mcherry-eGFP-RAMP4 was recombined with pInd20 to create pInd20-mcherry-eGFP-RAMP4.

2.3. Cell lines, cell culture, transfection

HeLa Kyoto (in the following called HeLa) and HEK293T cells were maintained in Dulbecco's modified Eagle Medium + GlutaMax supplemented with 10% FBS and incubated at 37 °C, 95% relative humidity and 5% CO_2. Cells were transfected using Lipofectamine 2000 according to manufacturer's instruction.

2.4. Neuronal cell culture and transfection

Cortical neurons were isolated from wildtype murine embryonic brains (E15.5) of mixed brackground (FVB/NJ, C57BL/6, 129/Sv) and maintained in glia-conditioned neurobasal medium. Briefly, meninges were removed, cortices were isolated, minced and dissociated in trypsin solution for 15 min at 37 °C. The supernatant was removed and the tissue was washed 3 times with trituration solution (10 mM HEPES, 1% penicillin/streptomycin, 10 mM L-glutamine, 1% BSA, 10% FBS, 0,008% DNase in HBSS) and homogenized in trituration solution using fire polished glass pipettes. Finally, 200 000 cells were seeded on 6 cm plates containing poly-L-lysine coated coverslips and 4 ml glia-conditioned plating medium (1% penicillin/streptomycin, 1 mM sodium pyruvate, 0,5% glucose, 10 mM HEPES 1× B27 supplement, 10% FBS, 10 mM L-glutamine in MEM). Coverslips were washed with ethanol and sterilized at 240 °C prior to coating. After 24 h the plating medium was substituted by glia-conditioned neurobasal medium (10 mM HEPES, 1× B27 supplement, 5 mM L-glutamine in NBM). For preparation of glia-conditioned medium, a primary astroglia culture was established. For this purpose, brains were isolated from 15.5 days old embryos, the meninges were removed, the cerebral hemispheres were minced and afterwards dissociated in trypsin solution for 15 min at 37 °C. Finally, the tissue was homogenized by pipetting and cells were plated on a 10 cm dish containing glia medium (1% penicillin/streptomycin, 1 mM sodium pyruvate, 0,5% glucose, 10 mM HEPES, 20 mM L-glutamine, 10% FBS in MEM) and grown to confluency. For preconditioning of neurobasal medium or plating medium, the media were added to the glia feeder cultures and collected after 24 h.

For transfection, the calcium-phosphate method was used as described (Jiang and Chen, 2006) with the following changes: DNA-calcium phosphate-precipitates were prepared by mixing 80 ng/µl plasmid DNA and 250 mM $CaCl_2$ with equal volumes of 2 × BES buffered saline. Coverslips with attached neurons were transferred to a dish containing transfection medium (800 µM sodium pyruvate, 8 mM HEPES, 0.16% glucose, 5.5% ddH_2O in MEM, pH 7.65) and DNA precipitates were added. Subsequently, neurons were incubated at 37 °C for 1 h 30 min. Afterwards, neurons were incubated for 10 min in washing medium (800 µM sodium pyruvate, 8 mM HEPES, 0.16% glucose, 5.5% ddH_2O in MEM, pH 7.35) and moved back to their original dish containing glia-conditioned neurobasal medium. After 24 h, neurons were processed for immunocytochemistry.

2.5. Lentiviral transduction

HEK293T cells were used for virus production. Cells were co-transfected with 10 µg psPAX2, 5 µg pMD2.G and 20 µg lentiviral vector using PEI. Viral supernatant was harvested 48 h after transfection. For infection of HeLa cells, the filtered viral supernatant was diluted with culture medium supplemented with 7,5 µg/ml Polybrene. Infectious supernatant was removed after 24 h and selection of infected cells was started after 48 h.

2.6. Cell treatments

To depolymerize actin filaments, neurons were treated with 4 µM Cytochalasin D in DMSO or 5 µM Latrunculin A in DMSO for indicated time points. To depolymerize microtubules, neurons were treated with 2 µg/ml Nocodazole in DMSO for 1 h. To block autophagosome clearance, neurons were treated with 50 µM Chloroquine in PBS for 3 h. For detergent extraction experiments, neurons were washed briefly with PBS and then incubated with 0,05% Triton X-100 for 5 min at RT. Afterwards, neurons were washed twice with PBS and processed for immunofluorescence.

2.7. Immunocytochemistry and microscopy

Immunofluorescence staining was performed using standard protocols (Wacker et al., 1997) with the following changes: unspecific binding sites were blocked by incubation in blocking medium (1% BSA, 1% FBS, 0,1% fish gelatin). Primary and secondary antibodies were

diluted in blocking medium. For visualizing axonal autophagosomes, neurons expressing fluorescently-tagged autophagosome markers and ATL3 constructs were fixed and directly mounted. Images were acquired on a Zeiss Axiovert200 (Zeiss, Jena, Germany) using 20 ×, 40 × or 63 × objective and Zen2012 software. Images were assembled and processed in Zen2012 and Adobe Photoshop. Care was taken that identical settings were applied where images were to be compared. Weak signals like axonal autophagosomes or lysosomes were enhanced using gamma settings <1 to match the image perception by eye.

2.8. Expansion microscopy

Expansion microscopy was performed using an adapted protocol from Chozinski et al. (Chozinski et al., 2016). Cells were fixed and stained as outlined above. After secondary antibody staining, cells were washed two times with PBS and incubated with 1 mM methacrylic acid N-hydroxysuccinimide ester for 1 h. Afterwards, the cells were washed two times with PBS and incubated in monomer solution (1× PBS, 2 M NaCl, 2.5%, acrylamide, 0.15% *N*,*N*′-methylenebisacrylamide, 8.6% sodium acrylate) for 1 min. The gelation chamber was prepared by placing 3 cover glasses with a drop of water in between on top of each other on both sides of an object holder leaving a gap in the middle. The coverslip containing stained and postfixed cells was placed in the middle of the object holder with cells facing upwards. 200 µl of gelation solution (1× PBS, 2 M NaCl, 2.5%, acrylamide, 0.15% *N*,*N*′-methylenebisacrylamide, 8.6% sodium acrylate, 0,2% APS, 0,2% TEMED were pipetted on top of the sample. The gelation chamber was sealed by placing a long coverglass on top and polymerization was carried out for 30 min at RT. The coverglass was carefully removed and the gel containing the cells was separated from the coverslip using a razorblade. The gel was placed in digestion solution (0,5% Triton X-100, 0,8 M guanidine HCL, 8 U/ml Proteinase K in 1× TAE) and incubated for 30 min at RT. Afterwards, the gel was placed in a 6 cm glass bottom dish containing ddH2O with cells facing downwards for expansion. The water was exchanged every 30 min for 2 h. Subsequently, the water was removed and the expanded cells inside the gel were imaged on a Zeiss Axiovert200 microscope using a 40 × objective. Images were assembled and processed in Zen2012 and Adobe Photoshop. Care was taken that identical settings were applied where images were to be compared. Weak signals like axonal ER tubules were enhanced using gamma settings <1 to match the image perception by eye.

2.9. ER-phagy analysis

HeLa cells were transduced with lentiviral particles and selected to stably express pInd20-mcherry-eGFP-Ramp4. 48 h prior to imaging, cells were treated with Doxycycline (1 µg/ml) to induce mcherry-eGFP-Ramp4 expression. Cells were then transfected with BFP-ATL3 or BFP-ATL3 Y192C and live cell imaging was performed 24 h later.

2.10. Quantification of immunocytochemistry

The number of axonal autophagosomes and lysosomes was quantified manually using Zen2012 software. To quantify the relative intensity of ATL3 and ATL3 Y192C within the AIS a freehand line was drawn along the AIS and intensities along the line were measured using ImageJ. The resulting signal intensity profiles of single neurons were averaged and normalized to the first value. To determine the ratio of axonal ATL3 and different ER markers, axonal lengths of signals were measured manually using ImageJ. To analyze the ER-phagy rate, autolysosomes containing mcherry-eGFP-RAMP4 were quantified. Since eGFP is quenched in the acidic environment, the autolysosomes appear red. To count these structures a self-written ImageJ Macro was used (Supplemental information). Briefly, the green channel was subtracted from the red channel and the resulting red autolysosomes were quantified.

2.11. FRAP

FRAP experiments were performed essentially as described before (Diekmann and Hoischen, 2014; Hemmerich et al., 2008). Here we used the fast Airyscan super resolution mode (16 phases) on a Zeiss LSM 880 microscope (Zeiss, Jena, Germany) equipped with an Airyscan detector using a C-Apochromat 40×/1.2 N.A. W Korr objective. eGFP was excited with a 488 nm Argon laser line using MBS 488 and the emission was captured through an SBS BP 420–460 + LP 500 in combination with emission filter BP 420–480 + BP 495–550. Pixel size in fast Airyscan super resolution mode acquisition was applied automatically in ZEN 2.3 software for the eGFP channel, usually resulting in a pixel size of 40 × 40 nm. 5 images were taken before the bleach pulse and 200 images after bleaching (70 iterations with 100% laser intensity) of a rectangular region, which was for all experiments of the same size and shape, covering a small area of the cytoplasmic ER. The image acquisition frequency was set to 1 frame/s at 1% laser transmission, a zoom of 10, a pixel dwell of 0,59 µs, and a line average of 1. After processing of the raw fast Airyscan data the quantitation of relative fluorescence intensities was done using Sigma Plot software. Recovery half-times and residence times were determined from FRAP data as described previously (Bulinski et al., 2001; Hemmerich et al., 2008).

2.12. Live cell imaging

To image the ER in living neurons, we used the fast Airyscan super resolution mode (16 phases) on a Zeiss LSM 880 microscope (Zeiss, Jena, Germany) equipped with an Airyscan detector using a C-Apochromat 40×/1.2 N.A. W Korr objective. eGFP was excited with a 488 nm Argon laser line using MBS 488 and the emission was captured through an SBS BP 420–460 + LP 500 in combination with emission filter BP 420–480 + BP 495–550. Pixel size in fast Airyscan super resolution mode acquisition was applied automatically in ZEN 2.3 software for the eGFP channel, usually resulting in a pixel size of 50 × 50 nm.

2.13. Cell lysis, co-immunoprecipitation, Western blot

For co-immunoprecipitation experiments, HEK293T cells were lysed in CHAPSO lysis buffer (2% CHAPSO in 150 mM citrate buffer, pH 6.4 and protease inhibitor mix). Lysates diluted to 1% CHAPSO concentration were incubated with GFP-Trap or myc-Trap agarose beads o/n on a rotating wheel at 4 °C. Beads were washed two times with 0,5% CHAPSO in 150 mM citrate buffer, pH 6.4 and once with 150 mM citrate buffer, pH 6.4. Afterwards beads were boiled in Laemmli buffer. Eluted proteins were separated by SDS-PAGE, transferred to PVDF membranes and probed with antibodies as indicated.

2.14. Blue Native PAGE

For Blue Native PAGE experiments, HeLa cells were lysed in digitonin lysis buffer (1% digitonin, 20 mM Tris/HCL pH 7.4, 0,1 mM EDTA, 50 mM NaCl, 10% glycerol and protease inhibitor mix). Subsequently 10× sample buffer (5% Coomassie Brilliant Blue G-250, 100 mM Bis-Tris pH 7.0, 0,5 mM 6-aminocaproic acid) was added to a final 1× concentration and samples were incubated on ice for 10 min. Afterwards samples were loaded on precast Native PAGE 4–16% BisTris gels. Cathode buffer (50 mM Tricine, 7,5 mM imidazole, 0,02% Coomassie Brilliant Blue G-250, pH 7.0) and anode buffer (25 mM imidazole, pH 7.0) were added and proteins were separated at 150 V. After 60 min the cathode buffer was exchanged to cathode buffer without Coomassie Brilliant Blue G-250 and separation was carried on at 250 V. Proteins were transferred to PVDF membranes and excess Coomassie Brilliant Blue G-250 was removed by incubating the membrane with methanol. Subsequently, membranes were blocked and probed with antibodies as indicated.

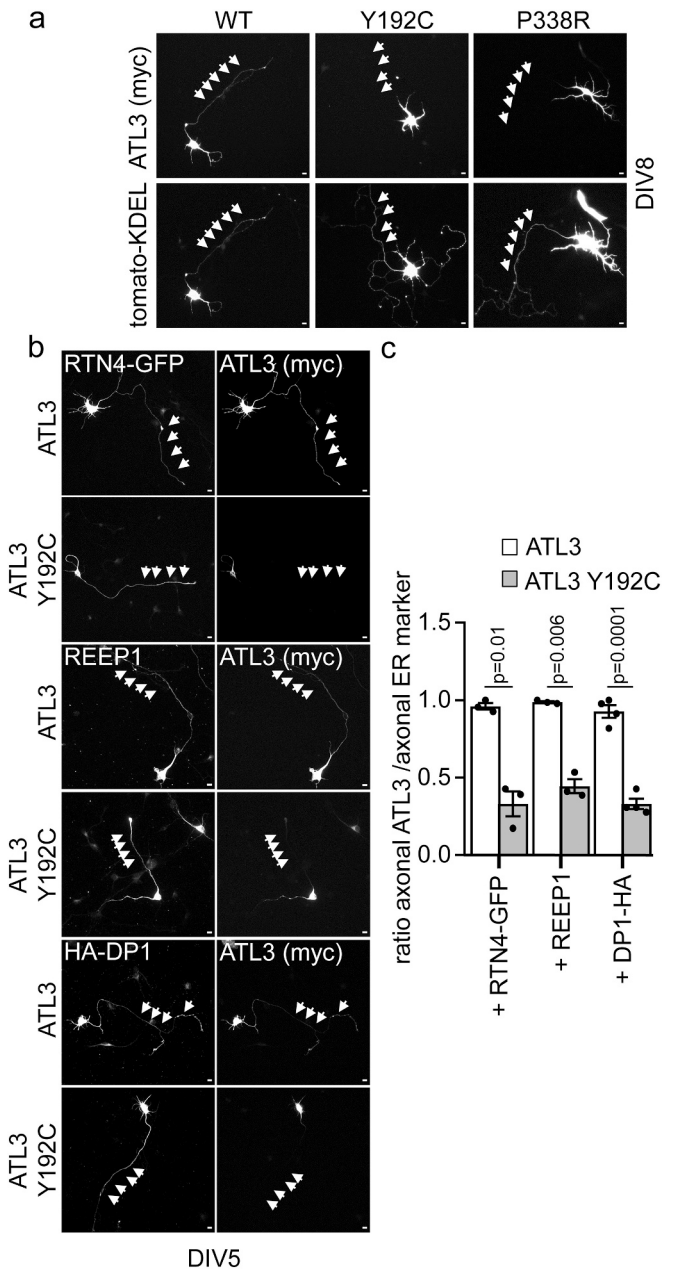

Fig. 1. Mutated ATL3, but not unrelated ER-membrane proteins are excluded from axonal ER. Primary cortical murine neurons were transfected with myc-tagged ATL3 variants together with tomato-KDEL (a) or RTN4-GFP or HA-DP1 or REEP1 (b), fixed 24 h later and stained with antibodies as indicated. The days of culturing – days in vitro (DIV) at day of fixation are indicated. Arrows point to axons. c) Quantification from b. The ratio depicts the mean length of axonal ATL3 staining divided by the mean length of the axonal ER extending into the axon. Analyzed were 35–47 neurons for each condition from at least three independent experiments. Error bars depict SEM, *p* values are indicated (Welch's *t*-test). Scale bar 10 μm.

2.15. Statistics

Reported values represent mean ± SEM, unless stated otherwise. Statistical differences between the means of two groups were determined using Welch's *t*-test. Numbers of independent replicates and *p* values are indicated in figures or figure legends, a p value < 0.05 was considered significant.

3. Results

3.1. ATL3 Y192C and P338R, but not unrelated ER membrane proteins, are excluded from axonal ER

We have previously shown that neuronal ATL3 Y192C extends only into proximal axonal segments, while a lumenal ER marker, tomato-KDEL, localizes also to distal axonal regions (Behrendt et al., 2019). This suggests a localization defect of mutated ATL3 rather than a general malformation or discontinuity of the axonal ER. It remained open if this was a specific effect of ATL3 Y192C or a general phenomenon of ATL3 mutants. We therefore transfected ATL3 or ATL3 Y192C or P338R in DIV (day in vitro) 8 cortical neurons together with a marker for lumenal ER, tomato-KDEL (Fig. 1a). Both ATL3 Y192C and P338R were excluded from axons, whereas ATL3 and the lumenal ER-marker localized along the whole axon. Additionally, ATL1 Y196C, which causes hereditary spastic paraplegia (McCorquodale 3rd et al., 2011), is also excluded from the axon (Suppl. Fig S2:) suggesting that axonal exclusion is a general phenomenon for mutated ATLs. Since both ATL3 mutations behaved identical, we focused on ATL3 Y192C. To analyze if expression of ATL3 Y192C leads to a general mislocalization of axonal ER membrane proteins, we transfected RTN4A-GFP, DP1-HA or REEP1 in DIV4 neurons together with ATL3 or ATL3 Y192C, fixed and stained the cells 24 h later (Fig. 1 b,c). As expected, all analyzed axonal ER membrane proteins were present in distal axonal regions when co-expressed with ATL3. Likewise, expression of ATL3 Y192C did not lead to axonal exclusion of RTN4A, DP1 or REEP1, indicating that the mutant ATL3 does not induce a general transport block into the axon. Co-immunoprecipitation experiments in HEK293T cells show that ATL3 as well as ATL3 Y192C interact with REEP1, RTN4A and DP1 (Suppl. Fig. S1), eliminating the possibility that mutant ATL3 is excluded from the axonal ER due to absent interaction with other ER membrane proteins. Collectively, the data confirm the exclusion of mutant ATL3 from axons with an intact axonal ER, pointing at a specific mechanism that traps mutant ATL3 in proximal axonal segments.

3.2. ATL3 Y192C displays reduced mobility in ER membranes

To test if axonal ATL3 Y192C exclusion is caused by aggregation and/or a reduced mobility in ER membranes, we determined the lateral diffusion of GFP-ATL3 or GFP-ATL3 Y192C in the somatic ER of DIV6–8 neurons using a fluorescence recovery after photobleaching (FRAP) approach (Fig. 2). For this analysis, regions with comparable ER density were bleached. GFP-ATL3 recovered with a halftime of 4,7 s, comparable to other ER membrane proteins (Nehls et al., 2000; Pawar et al., 2017). In contrast, the halftime of GFP-ATL3 Y192C was almost tripled to 13,3 s, indicating a reduced lateral mobility of GFP-ATL3 Y192C in the ER membrane (Fig. 2a, b). ATLs homodimerize to mediate ER tubule fusion (Orso et al., 2009). To examine if ATL3 Y192C oligomers or aggregates reduce lateral diffusion, we performed Blue Native PAGE (Fig. 2c). The non-denaturing conditions of this method allow the visualization of ATL3 monomers, dimers and, if present, higher order complexes. ATL3 and ATL3 Y192C exhibited similar monomer/dimer ratios and higher order complexes or aggregates were not detectable in both cases. This suggests that the lateral mobility of ATL3 Y192C is not reduced by higher order oligomers/oligomerization. Although ATL3 Y192Cs lateral mobility is reduced almost 3-fold compared to ATL3, this cannot account for its axonal exclusion: ATL3 Y192C was evenly distributed in long dendrites (Fig. 2d), suggesting neurite length is not a restricting factor for ATL3 Y192C distribution. Furthermore, the recovery time we determined is still within seconds, meaning that ATL3 Y192C would have reached the distal axonal ER eventually after the 24 h between transfection and fixation. Therefore, we hypothesized that a barrier at the soma or proximal axon limits the axonal entry of ATL3 Y192C.

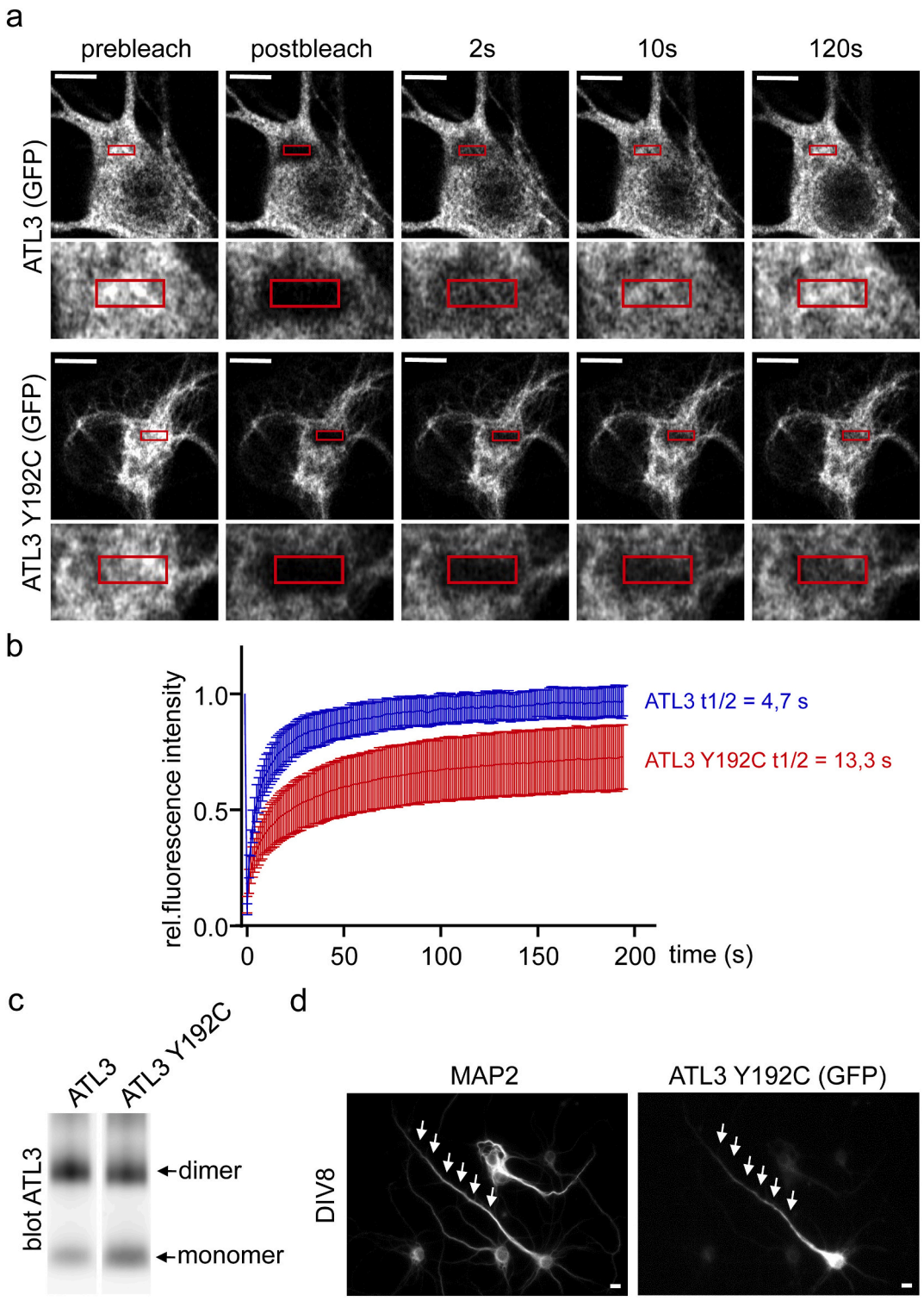

Fig. 2. ATL3 Y192C displays a reduced mobility within the ER. a) FRAP analysis of GFP-ATL3 and GFP-ATL3 Y192C diffusion in the somatic ER. Primary cortical murine neurons (DIV5–7) were transfected with GFP-tagged ATL3 variants. After 24 h, regions of interest (ROI) in the somatic ER (red boxes) were photobleached and recovery rates of GFP-ATL3 or GFP-ATL3 Y192C were determined. The lower rows show the ROIs at a higher magnification. Scale bar: 10 μm. b) GFP-ATL3 and GFP-ATL3 Y192C recovery dynamics. Data points show mean ± s.d. ($n = 58$ and 55 neurons for GFP-ATL3 and GFP-ATL3 Y192C expressing cells, respectively, from 8 independent experiments). c) Blue Native PAGE to visualize ATL3 monomers and dimers. HeLa cells were transfected with myc-tagged ATL3 variants, lysed 24 h later, separated under non-denaturing conditions, transferred to PVDF membranes and processed for immunoblotting with anti-ATL3 antibodies. ATL3 monomers and dimers are indicated. A representative blot from $n = 3$ independent experiments is shown. Full-size blots are shown in Suppl. Fig. S6. d) Mutant ATL3 can enter distal dendrites. Primary cortical murine neurons were transfected with GFP-ATL3 Y192C, fixed 24 h later and stained with MAP2 antibodies as marker for dendrites. The DIV at day of fixation is indicated. Arrows point to dendrites. Scale bar: 10 μm. Analyzed were 28 neurons from three independent experiments. (For interpretation of the references to colour in this figure legend, the reader is referred to the web version of this article.)

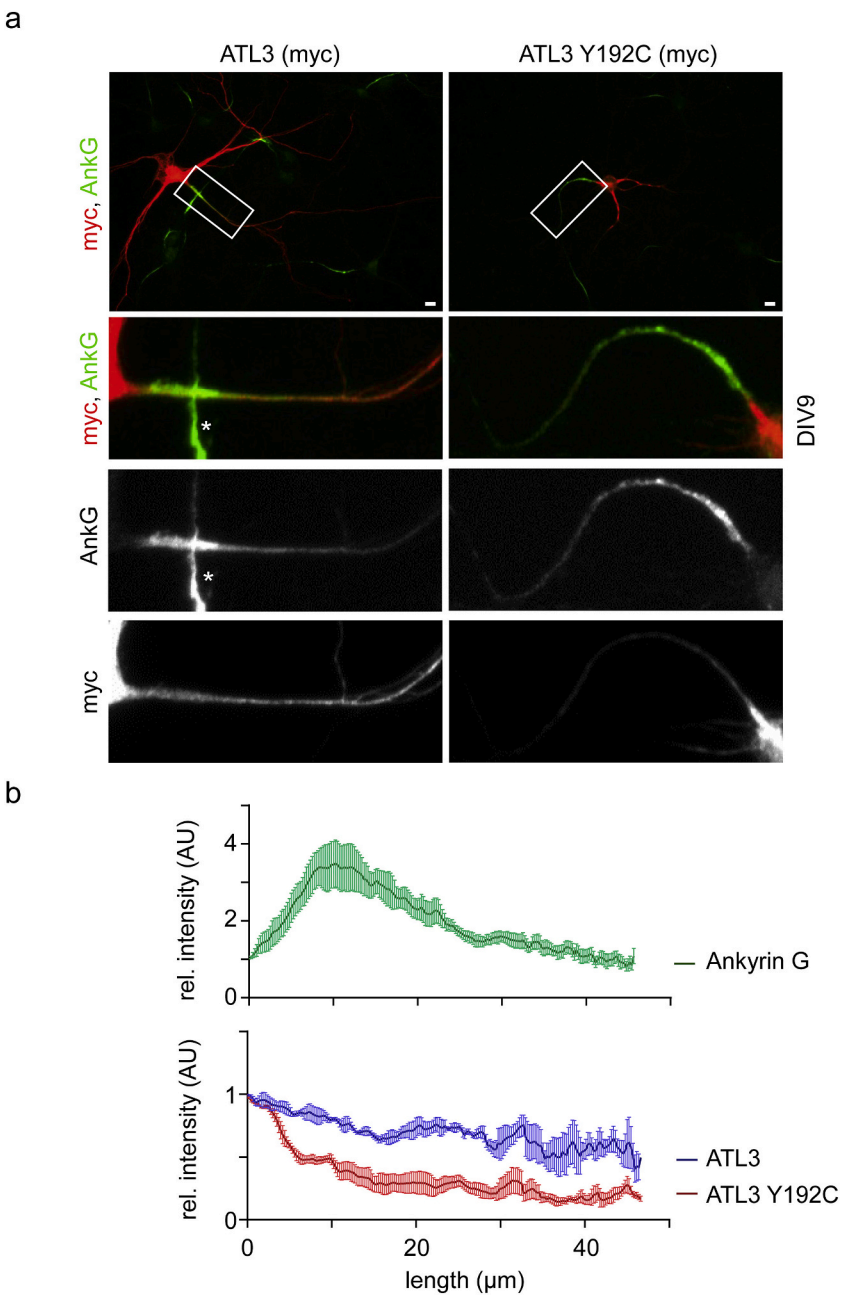

Fig. 3. A barrier for ATL3 Y192C at the AIS. a) Primary cortical murine neurons were transfected with myc-tagged ATL3 variants, fixed 24 h later and stained with antibodies against myc and AnkyrinG (AnkG, a marker for the AIS) indicated. The boxed area around the AIS is shown at a higher magnification. The asterisk indicates an AIS from an untransfected, neighbouring neuron. The DIV at day of fixation is indicated. Scale bar: 10 µm. b) Quantification from a). Intensities along the AIS were analyzed using curve scans. Data points show mean + SEM. Analyzed were 28–32 neurons for each condition from three independent experiments.

3.3. A barrier for ATL3 Y192C at the axon initial segment

The axon initial segment (AIS) acts as a gate between the somatodendritic compartment and the axon (Huang and Rasband, 2018; Leterrier, 2018). To investigate a potential involvement of the AIS in excluding ATL3 Y192C from the axonal ER, we stained the AIS marker AnkyrinG (AnkG) in DIV8 neurons that express myc-ATL3 or myc-ATL3 Y192C (Fig. 3a). Using curve scans, the intensity of ATL3 or ATL3 Y192C along the AIS was analyzed (Fig. 3b). While the ATL3 intensity decreased slowly and linear throughout the AIS and beyond, the ATL3 Y192C signal declined sharply at the proximal end of the AIS, where the AnkG signals peaked, and was hardly detectable distal to the AnkG peak and beyond. The data suggest the presence of a diffusion barrier for mutated ATL3 at the AIS. The barrier function is not mediated by a strong interaction of AnkG and ATL3 Y192C, trapping the latter at the AIS. This was demonstrated by detergent extraction experiments where AnkG but not ATL3 or ATL3 Y192C exhibited detergent resistant properties (Figure Suppl. Fig. S3:). Taken together, a barrier at the AIS prevents ATL3 Y192C but not ATL3 to enter the axon by a so far unknown mechanism.

3.4. Lack of axonal ATL3 does not change the axonal ER morphology

Imaging the ER in the narrow axon using light microscopy is challenging. This complicates the studies of mutated ER shaping proteins and their effect on axonal ER structure and function. To overcome this hurdle, we adapted an expansion microscopy protocol (Chen et al., 2015a; Chozinski et al., 2016) to physically magnify the sample. Expanding DIV8 neurons resolved the structure of the axonal ER marked by GFP-Sec61b (Fig. 4a). It forms a primarily tubular network consisting of 1–4 tubules that are occasionally connected, in line with data acquired by serial-section electron microscopy (Terasaki, 2018). Interestingly, we found that the ER complexity, i.e. the number of ER tubules, is reduced within the AIS, maybe where the diffusion barrier is located

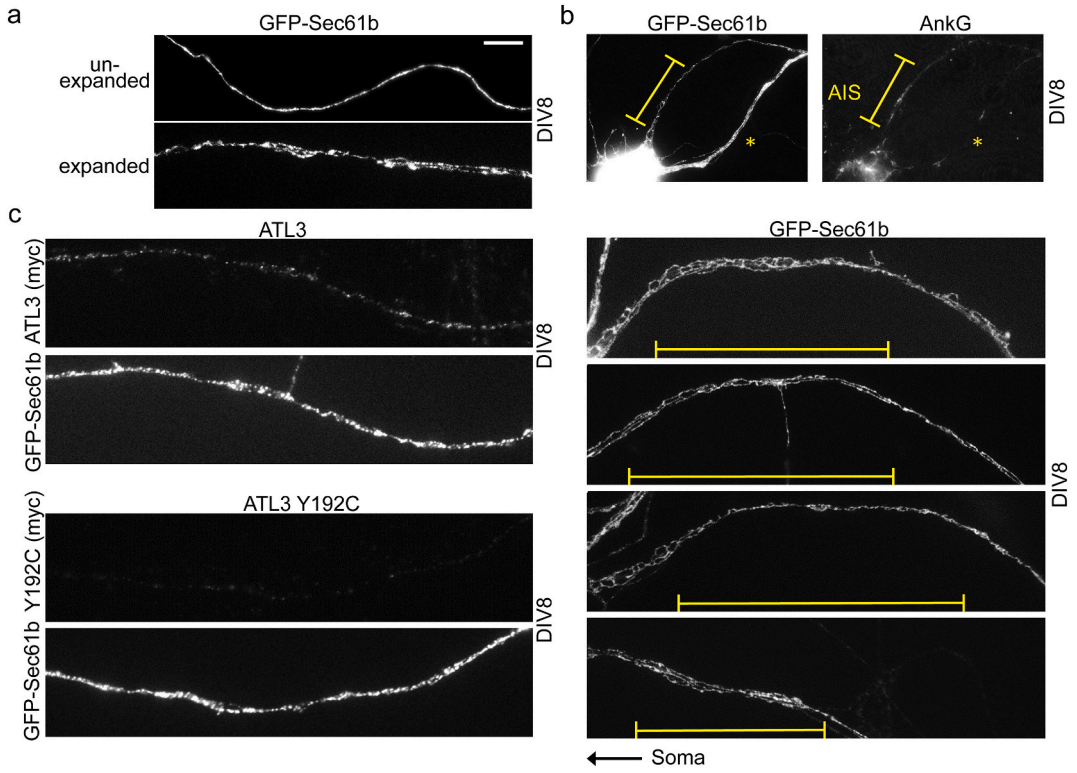

Fig. 4. Axonal ER visualized by expansion microscopy. Primary cortical murine neurons were transfected with GFP-Sec61b or ATL3 variants, fixed 24 h later, stained with antibodies against AnkyrinG (AnkG) or myc as indicated, subjected to gelation and expansion (except a), top) and imaged. The DIV at day of fixation is indicated. a) Visualization of axonal ER-tubules without (top) and after expansion (lower image). Scale bar 10 μm b) ER complexity is reduced within the AIS. The AISs are marked by yellow lines. For clarity, the AnkG channel is only shown in the top panel. The asterisk marks a dendrite. Analyzed were 30 neurons from three independent experiments. 4 representative neurons are shown. c) Expression of ATL3 Y192C does not lead to changes in axonal ER morphology. Analyzed were 17 neurons for each condition from 13 independent experiments. One representative axon for ATL3 and ATL3 Y192C is shown, respectively. Scalebars for b-c) are waived, the expansion can only be estimated and is about four-fold.

(Fig. 4b).To analyze the impact of ATL3 exclusion on the axonal ER morphology, neurons co-expressing GFP-Sec61b and myc-ATL3 or myc-ATL3 Y192C were expanded and imaged. ATL3 is evenly distributed in the axonal ER, whereas ATL3 Y192C is absent from it (Fig. 4c). The exclusion of ATL3 Y192C (and thereby wildtype ATL3, see Fig. 6) has no visible effect on the morphology of the ER in the AIS or in distal axons. Since it was not possible to image three colours in expanded samples, it remains to be shown whether the area in the AIS, where the complexity of the ER is reduced, coincides with the barrier beyond which ATL3 Y192C is excluded.

3.5. *Depolymerizing the actin cytoskeleton allowed axonal entry of ATL3 Y192C*

To examine if the cytoskeleton is involved in excluding ATL3 Y192C from the axonal ER at the AIS, we transfected neurons with myc-ATL3 or myc-ATL3 Y192C together with RTN4A-GFP as a marker for axonal ER. Neurons were then treated with Latrunculin A or Cytochalasin D for 4 h to depolymerize the actin cytoskeleton (Fig. 5, Suppl. Fig. S4:) or with Nocodazole for 1 h to depolymerize microtubules (Fig. S5). Latrunculin A or Cytochalasin D effectively depolymerized actin filaments (Suppl. Fig. S4a) but had no influence on the distribution of the axonal ER marker RTN4A-GFP or myc-ATL3 along the axon (Suppl. Fig. S5:). Strikingly, however, disrupting the actin cytoskeleton for 4 h led to an entry of myc-ATL3 Y192C into the axonal ER (Fig. 5a). Actin depolymerization did not result in a full rescue of the ATL3 Y192C distribution into the axon, but the axonal ATL3 Y192C/ axonal ER ratio significantly increased from 0,2 to 0,5 (Fig. 5b). In contrast, disrupting microtubules had no effect on the distribution of RTN4A-GFP and ATL3 and also no effect on the exclusion of ATL3 Y192C from the axonal ER (Suppl. Fig. S5). These experiments indicate that the diffusion barrier for ATL3 Y192C at the AIS is directly or indirectly actin-dependent.

3.6. *Lack of axonal ATL3 results in fewer axonal autophagosomes and lysosomes*

We hypothesized that in neurons expressing mutated ATL3 Y192C also endogenous ATL3 would be excluded from the axonal ER, because both can dimerize with each other. Furthermore, in patients ATL3 Y192C acts dominant negative, suggesting that the non-mutated allele is also affected. To test this hypothesis, we transfected DIV7 neurons with GFP-ATL3 alone or together with myc-ATL3 Y192C, fixed them 24 h later and analyzed the GFP-ATL3 distribution in the axon (Fig. 6a). As expected, GFP-ATL3 was present in distal axons when expressed alone. Upon co-expression of myc-ATL3 Y192C however, GFP-ATL3 did not localize to distal axons, suggesting that it is excluded from axons by binding to mutant ATL3 (Fig. 6a). Co-immunoprecipitation experiments in HEK293T cells confirmed that overexpressed GFP-ATL3 interacts with myc-ATL3 Y192C (Fig. 6b). Additionally, both GFP-ATL3 and GFP-ATL3 Y192C interact with endogenous ATL3, suggesting that overexpression of ATL3 Y192C in neurons would also lead to an axonal exclusion of endogenous ATL3. Due to lack of functional antibodies against ATL3 we could not assay the absence of endogenous ATL3 in axons.

What is the functional consequence of the absence of axonal ATL3? The ER in the distal axon is important for autophagosome biogenesis (Maday et al., 2012b). Patient cells with one ATL3 Y192C allele displayed an autophagy defect (Behrendt et al., 2019) and ATL3 is involved in ER-phagy (Chen et al., 2019; Liang et al., 2018). This raised the question if the absence of ATL3 in axons affects axonal autophagosomes. To test this, DIV4 neurons were transfected with mRFP-LC3 and GFP-

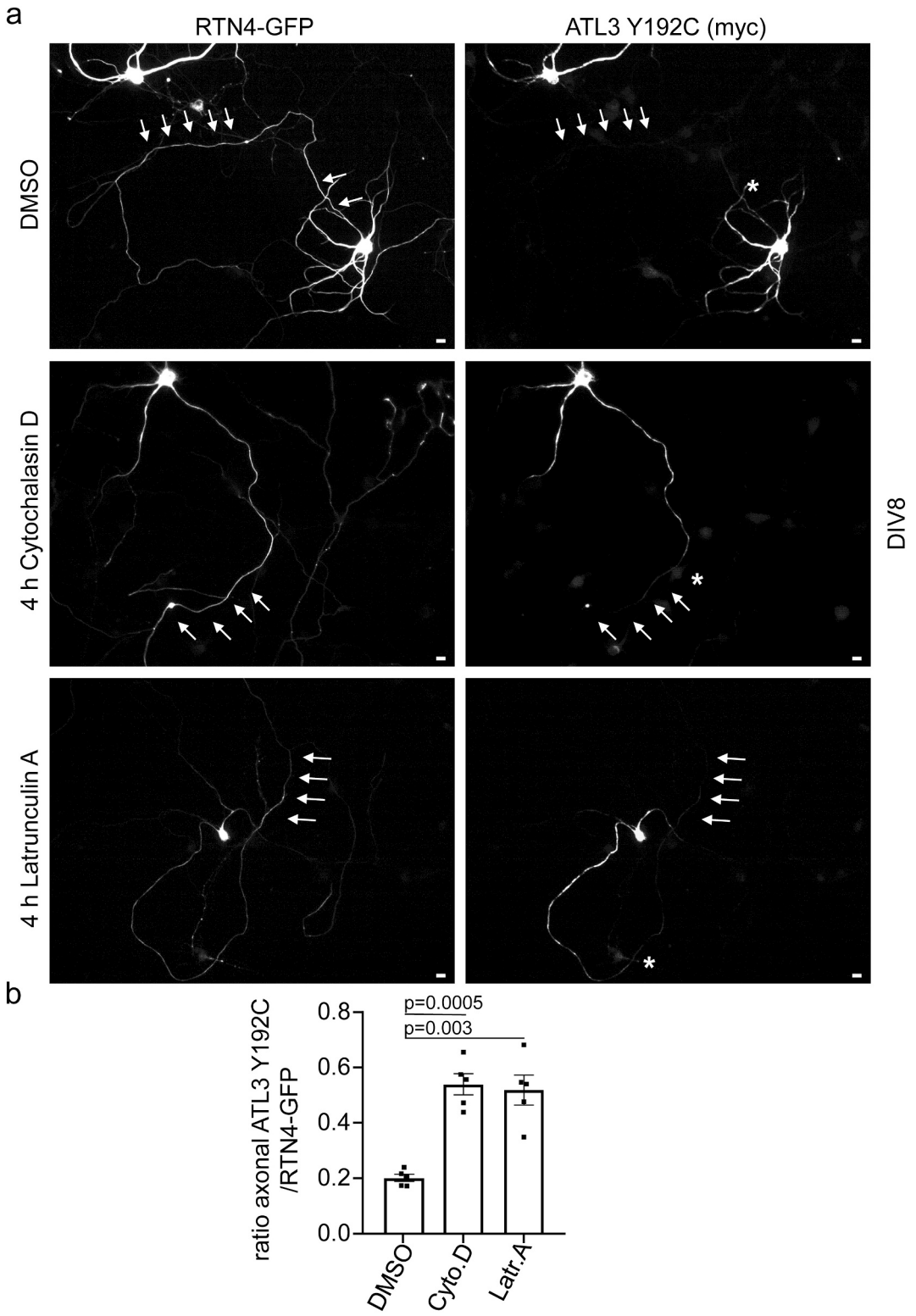

Fig. 5. Depolymerizing the actin cytoskeleton permits axonal entry of ATL3 Y192C. a) Primary cortical murine neurons were transfected with myc-ATL3 Y192C together with RTN4-GFP, incubated for 24 h, treated with DMSO or Cytochalasin D (4 μM) or Latrunculin A (5 μM) for 4 h, fixed and stained with antibodies against myc. The DIV at day of fixation is indicated. Arrows point to axons. Asterisks mark the distal end of ATL3 Y192C distribution. Scale bar 10 μm b) Quantification from a). The ratio depicts the mean length of ATL3 Y192C staining divided by the mean length of RTN4-GFP staining extending into the axon. Error bars depict SEM, *p* values are indicated (Welch's *t*-test) Analyzed were 63–74 neurons for each condition from 5 independent experiments.

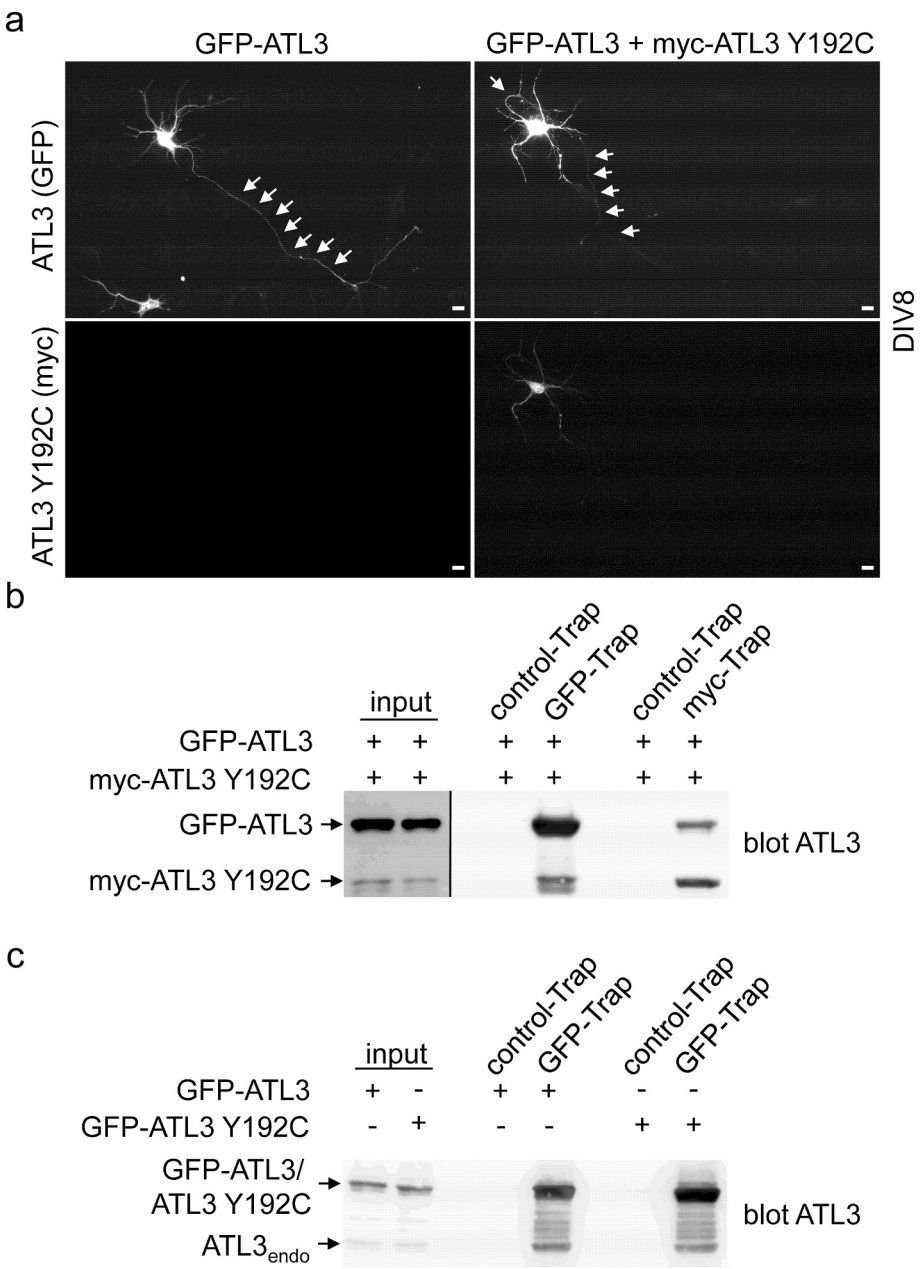

Fig. 6. ATL3 Y192C restricts ATL3 to the somatodendritic domain. a) Primary cortical murine neurons were transfected with GFP-ATL3 alone or together with myc-ATL3 Y192C, fixed 24 h later and stained with antibodies against myc. The DIV at day of fixation is indicated. Arrows point to axons. Scale bar 10 µm. Analyzed were 47–52 neurons for each condition from 5 independent experiments, representative images are shown. b) Co-immunoprecipitation experiments to show ATL3 interactions. HEK 293 T cells were transfected with GFP- or myc-tagged ATL3 variants as indicated and lysed 24 h later in CHAPSO lysis buffer. The lysates were incubated with GFP-Trap, myc-Trap or control beads as indicated and bound proteins were separated on SDS-PAGE, transferred to PVDF membranes and probed for ATL3. (n = 3 independent experiments). Full-size blots are shown in Suppl. Fig. S6.

ATL3 or GFP-ATL3 Y192C, fixed 24 h later and axonal autophagosomes (mRFP-LC3-positive vesicular structures) were counted (Fig. 7a, d). Expression of GFP-ATL3 Y192C resulted in a significant reduction of autophagosomes in the axon. Quantification of a different autophagosomal marker, DFCP1 (Derubeis et al., 2000), confirmed the decrease of axonal autophagosomes (Fig. 7b, e). Since ATL3 is involved in ER-phagy (Chen et al., 2019; Liang et al., 2018), is the reduction of axonal autophagy an indication of a reduced axonal ER-phagy? We were not able to get conclusive data in neurons, but in HeLa cells ATL3 Y192C significantly reduced ER-phagy (Suppl. Fig. S6). This suggests that in ATL3 Y192C expressing neurons axonal ER-phagy is impaired. Autophagosomes eventually fuse with lysosomes to autolysosomes (reviewed in Nakatogawa, 2020). We therefore analyzed axonal lysosomes that were labeled by LAMP1-RFP. Interestingly, expression of GFP-ATL3 Y192C also caused a significant decrease of axonal lysosomes (Fig. 7c, f).

Lysosomes are transported from the soma into the axon and a recent preprint highlights the importance of somatic ER tubules and ER-lysosome contacts for the transport of lysosomes into the axon (Özkan et al., 2020). ATL3 Y192C induced changes in somatic ER-morphology could therefore affect the numbers of axonal lysosomes. To analyze this further, we quantified the number of lysosomes in the AIS of DIV8 neurons expressing GFP-ATL3 or GFP-ATL3 Y192C and LAMP1-RFP (Fig. 8a,b). Expression of GFP-ATL3 Y192C reduced the number of lysosomes present in the AIS by almost 50%, suggesting that the reduction of axonal lysosomes could be caused by a decreased transport of lysosomes into the axon, possibly due to altered ER-morphology (Fig. 8c) and therefore altered ER-lysosome contacts.

In sum, the data indicate that lack of axonal ATL3 negatively affects the number of axonal autophagosomes while the ATL3 Y192C-induced ER-network deformation in the soma diminishes the number of axonal lysosomes. Both could contribute to axon degeneration in HSAN.

4. Discussion

In this study we show that HSAN-causing mutations Y192C and P338R in the ER-shaping protein ATL3 result in its exclusion from

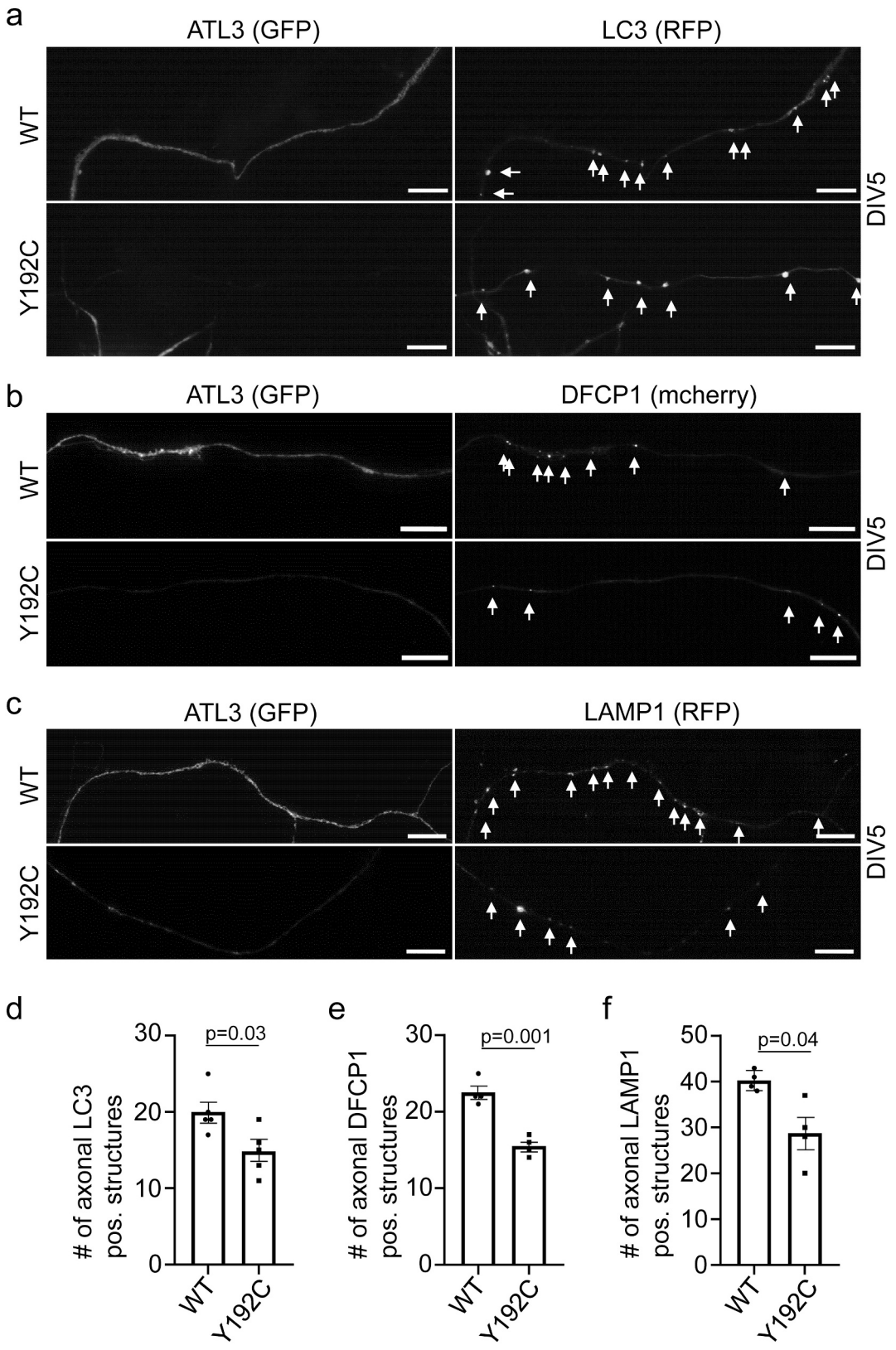

Fig. 7. Lack of axonal ATL3 results in fewer axonal autophagosomes and lysosomes. Primary cortical murine neurons were transfected with GFP-tagged ATL3 variants together with RFP-LC3 (a), mcherry-DFCP1 (b) or Lamp1-RFP (c), fixed 24 h later and imaged. The DIV at day of fixation is indicated. Axonal regions 50 μm apart from the soma are shown. Arrows point to autophagosomes and lysosomes, respectively. Scale bar 10 μm. d-f) Quantification from a-c; axonal autophagosomes and lysosomes were counted manually. Error bars depict SEM, *p* values are indicated (Welch's *t*-test). Analyzed were 49–78 neurons for each condition from at least 4 independent experiments.

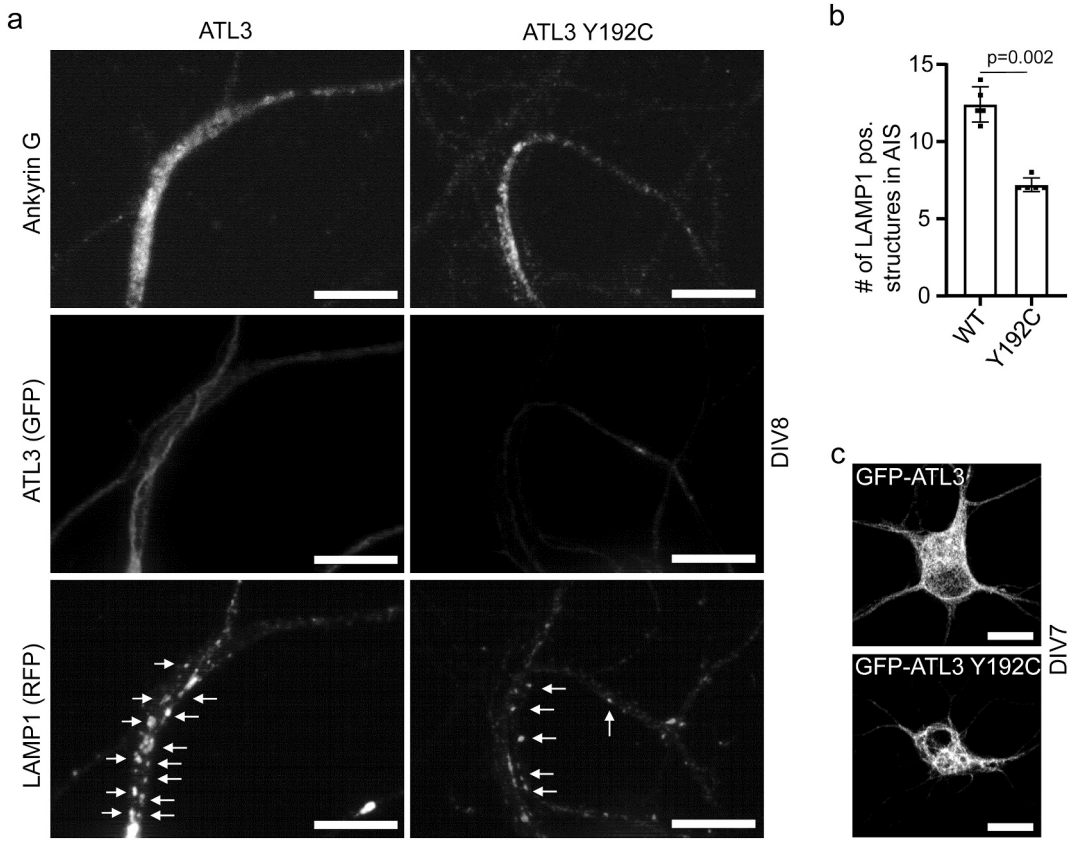

Fig. 8. Expression of ATL3 Y192C reduces the number of lysosomes in AIS. a) Primary cortical murine neurons were transfected with GFP-tagged ATL3 variants together with Lamp1-RFP, fixed 24 h later and stained with antibodies against AnkyrinG. The DIV at day of fixation is indicated. Arrows point to lysosomes. Scale bar 10 μm. b) Quantification from a). Lysosomes within the AIS were counted manually. Error bars depict SEM, *p* values are indicated (Welch's *t*-test). Analyzed were 67–73 neurons for each condition from 5 independent experiments. c) Primary cortical murine neurons were transfected with GFP-tagged ATL3 variants and analyzed 24 h later by live-cell microscopy using Airyscan-LSM.

axonal ER. A diffusion barrier at the AIS prevented mutant ATL1 and ATL3, but not unrelated membrane proteins, from transport into the axon. As a consequence, axonal autophagy, presumably including axonal ER-phagy, was reduced. In the soma the mutations caused disruption of the ER network, probably resulting in reduced ER-lysosome contacts and consequently a reduced lysosomal transport into the axon. Both effects suggest a possible novel pathomechanism for HSAN.

The findings presented here extend our knowledge about mutated ATL3. We and others previously showed that ATL3 Y192C overexpression has dramatic effects on the reticular ER-network in unpolarized cells (Behrendt et al., 2019; Kornak et al., 2014; Krols et al., 2018b). Pathogenic ATL3 variants are defective in membrane fusion, despite retaining their GTPase activity. This defect results in membrane tethering and aligning of long ER-tubules (Krols et al., 2018b). Functionally, the disrupted ER network results in delays in ER-Golgi transport (Behrendt et al., 2019; Niu et al., 2019) and reduced autophagy (Behrendt et al., 2019) or, according to a different study, increased autophagy (Krols et al., 2018a).

Interestingly, we here discovered that mutated Y192C and P338R ATL3 as well as ATL1 Y196C are selectively excluded from distal axons. The exclusion is not mediated by immobilization of ATL3 variants in the somatodendritic domain. Our FRAP experiments demonstrated a threefold lower mobility in ER-membranes of the soma, but this cannot explain the axonal exclusion. The reduced mobility does not prevent the mutant ATLs from traveling to distant dendrites several dozens of micrometers away from the soma. Also, the 24 h between the transfection and fixation would allow ample time for active or passive transport to distal locations in the axon several 100 μm away from the soma. If not reduced mobility, what then prevents ATL3 variants from entering axons? Close inspection of the fluorescent signal intensity of ATL3 Y192C revealed a sharp decline near the proximal end of the AIS, at a position close to the peak of AnkyrinG staining. Moreover, depolymerizing the actin, but not the microtubule cytoskeleton permitted access of ATL3 Y192C to the axon. These findings are in line with a concept of a diffusion barrier for selected ER-membrane proteins at the AIS, in analogy to the diffusion barriers for plasma membrane proteins, transport vesicles and soluble proteins at the AIS (reviewed in Huang and Rasband, 2018; Leterrier, 2018). Actin at the AIS forms concentric rings and is present in patches that prevent somatodendritic-destined transport vesicles to enter the axon (Leterrier, 2018), but how actin is involved in an ER-diffusion barrier will need further investigations. To our knowledge, our experiments provide the first evidence of a barrier for selected ER-membrane proteins at the AIS. Similar mechanisms might regulate the mobility of ER membrane proteins at dendritic branch points (Cui-Wang et al., 2012), but in both cases the mechanism remains elusive. Interestingly, a barrier for ER membrane proteins exists in *S. cerevisae*. Here, the ER membrane protein Scs2 together with the septin Shs1 forms a diffusion barrier between the ER of the mother and the ER of the bud (Chao et al., 2014). Scs2 is the yeast ortholog of the mammalian VAPB and future studies will show if septins and VAPB are involved in ER diffusion barrier at the AIS.

How could the absence of ATL3 Y192C from axons cause axonopathy? HSAN1F is a dominant-negative axonopathy. We hypothesize that two effects together contribute to the axonopathy: a) mutant ATL3 traps wild-type ATL3 and potentially also ATL1 and ATL2 in the somatodendritic domain. There it causes the striking rearrangements of the ER network that were also observed in non-neuronal cells (Behrendt et al.,

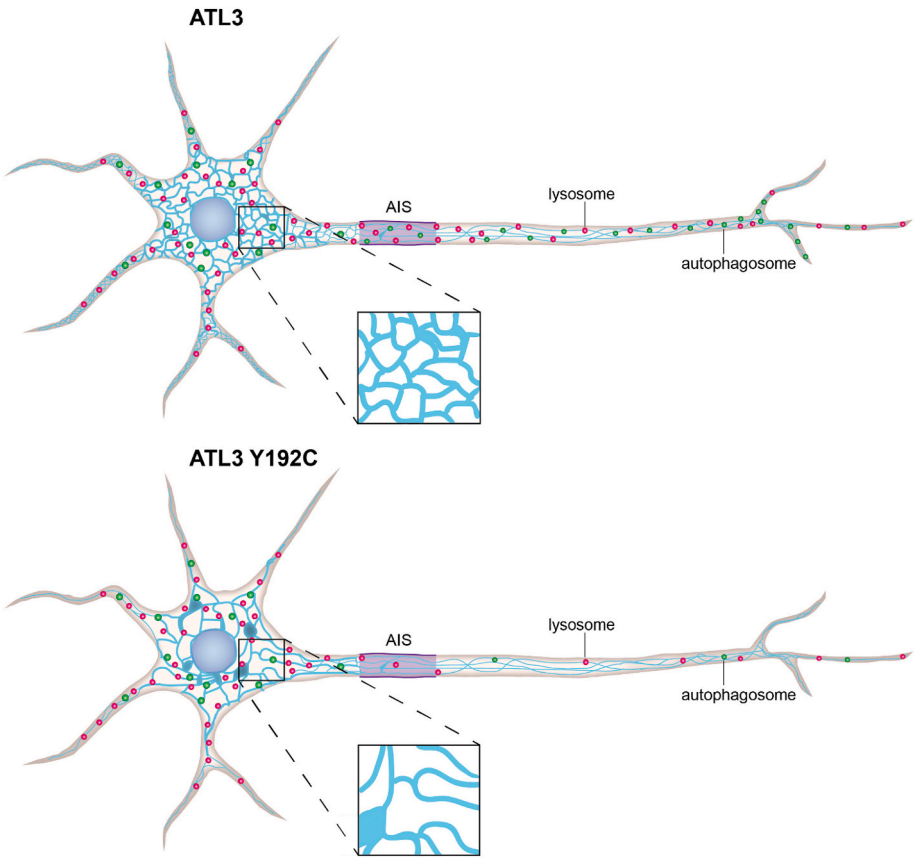

Fig. 9. Hypothetical pathomechanism of mutant ATL3 Y192C. Top, healthy neuron with intact ER-network and homeostatic distribution of lysosomes and autophagosomes. Bottom, disturbed somatic ER-network resulting in reduced ER-lysosomal contacts in the pre-axonal zone and absence of axonal ATL3. Both result in reduction in axonal lysosomes and autophagosomes, reflecting deficits in autophagy/ER-phagy that contributes to axonal degeneration.

2019; Kornak et al., 2014; Krols et al., 2018b). ER membrane tethering and the loss of 3WJs disturb ER-lysosome contacts in the recently discovered somatic pre-axonal zone where lysosomes are prepared for their delivery in axons (Özkan et al., 2020). This results in a net-loss of axonal lysosomes. b) In addition, because of the absence of ATLs in the distal axon, ATL3/GABARAP-mediated ER-phagy is reduced. A model schematizing our hypothesis is presented in Fig. 9. Additional mechanisms, like the effect of ATL3 Y192C expression on the distribution of axonal mitochondria, likely also contribute to the pathomechanism (Krols et al., 2018a).

The pivotal role of axonal autophagy for axonal homeostasis is widely appreciated, as are the consequences of a disturbed autophagic flux resulting in axon degeneration (reviewed in Overhoff et al., 2020; Stavoe and Holzbaur, 2019a; Stavoe and Holzbaur, 2019b; Wang et al., 2018). The axonal ER has multiple functions ranging from lipid synthesis, protein translation and folding to calcium dynamics and interacts functionally with the axonal plasma membrane, endosomes, mitochondria and autophagosomes (reviewed in Luarte et al., 2018). An imbalanced ER homeostasis, caused for example by a reduced ER-phagy, has been implicated in a number of neurological diseases (Roussel et al., 2013; Yamanaka and Nukina, 2018). Imbalanced ER homeostasis induced by structural changes plays an important role in length-dependent axonopathies like HSAN and hereditary spastic paraplegias (HSP)(Fowler et al., 2019; Ozturk et al., 2020). This is implied by the high incidence of ER-shaping and/or ER-phagy genes that are mutated in length-dependent axonopathies. Among these are REEP1, REEP2, ATL1, ATL3, ARL6IP1, RTN2, SPAST and FAM134B (reviewed in Hübner and Kurth, 2014; Wilkinson, 2019).

Our results presented here are in line with the proposed hypothesis. The cortical neurons we used are not the primary affected neuron type in HSAN1. However, also ATL1 Y196C, which causes degeneration of upper motor neurons (McCorquodale et al., 2011), is excluded from distal axons in cortical neurons. This suggests that the mechanism of selective axonal exclusion of mutated proteins is not restricted to ATL3. Future studies for example using mouse models of HSAN1F will have to demonstrate if indeed wild-type ATL3 is kept away from axons when mutated ATL3 is present. It also has to be tested if the reduced autophagy/ER-phagy is responsible for the axon degeneration and what the molecular mechanism of the ER-membrane diffusion barrier at the AIS is.

5. Conclusions

The data presented here describe for the first time the existence of a diffusion barrier in the ER at the AIS which selectively excludes mutant ATL3 from distal axons. The existence of such a barrier together with somatic malformations of the tubular ER-network causes a reduction of axonal lysosomes and autophagosomes. This imbalance in axonal homeostasis is suggestive of a pathomechanism of ATL-caused axonopathies.

Supplementary data to this article can be found online at https://doi.org/10.1016/j.nbd.2021.105400.

Declaration of Competing Interest

None.

Acknowledgements

We thank Daniela Reichenbach for excellent technical assistance in

primary neuronal culture and Patrick Lüningschrör, Christian Beetz, Justine Wagner, Christina Valkova and Ingo Kurth for plasmids. We greatly acknowledge the support by the FLI LGSA (to LB).

References

Ban, B.K., et al., 2013. Autophagy negatively regulates early axon growth in cortical neurons. Mol. Cell. Biol. 33, 3907–3919.

Beetz, C., et al., 2012. Exome sequencing identifies a REEP1 mutation involved in distal hereditary motor neuropathy type V. Am. J. Hum. Genet. 91, 139–145.

Behrendt, L., et al., 2019. A disease causing ATLASTIN 3 mutation affects multiple endoplasmic reticulum-related pathways. Cell. Mol. Life Sci. 76, 1433–1445.

Bulinski, J.C., et al., 2001. Rapid dynamics of the microtubule binding of ensconsin in vivo. J. Cell Sci. 114, 3885–3897.

Chao, J.T., et al., 2014. Polarization of the endoplasmic reticulum by ER-Septin tethering. Cell. 158, 620–632.

Chen, S.L., et al., 2012. ER network formation requires a balance of the dynamin-like GTPase Sey1p and the Lunapark family member Lnp1p. Nat. Cell Biol. 14, 707–716.

Chen, S.L., et al., 2013. ER structure and function. Curr. Opin. Cell Biol. 25, 428–433.

Chen, F., et al., 2015a. Optical imaging. Expansion microscopy. Science. 347, 543–548.

Chen, S., et al., 2015b. Lunapark stabilizes nascent three-way junctions in the endoplasmic reticulum. Proc. Natl. Acad. Sci. U. S. A. 112, 418–423.

Chen, Q.Z., et al., 2019. ATL3 is a tubular ER-Phagy receptor for GABARAP-mediated selective autophagy. Curr. Biol. 29, 846.

Chino, H., Mizushima, N., 2020. ER-Phagy: quality control and turnover of endoplasmic reticulum. Trends Cell Biol. 30, 384–398.

Chozinski, T.J., et al., 2016. Expansion microscopy with conventional antibodies and fluorescent proteins. Nat. Methods 13, 485–488.

Cui-Wang, T.T., et al., 2012. Local zones of endoplasmic reticulum complexity confine cargo in neuronal dendrites. Cell 148, 309–321.

Derubeis, A.R., et al., 2000. Double FYVE-containing protein 1 (DFCP1): isolation, cloning and characterization of a novel FYVE finger protein from a human bone marrow cDNA library. Gene. 255, 195–203.

Diekmann, S., Hoischen, C., 2014. Biomolecular dynamics and binding studies in the living cell. Phys Life Rev 11, 1–30.

Fimia, G.M., et al., 2007. Ambra1 regulates autophagy and development of the nervous system. Nature. 447, 1121–1125.

Fischer, D., et al., 2014. A novel missense mutation confirms ATL3 as a gene for hereditary sensory neuropathy type 1. Brain. 137, e286.

Fowler, P.C., et al., 2019. NeurodegenERation: the central role for ER contacts in neuronal function and axonopathy, lessons from hereditary spastic paraplegias and related diseases. Front. Neurosci. 13.

Friedman, J.R., et al., 2011. ER tubules mark sites of mitochondrial division. Science. 334, 358–362.

Hemmerich, P., et al., 2008. Dynamics of inner kinetochore assembly and maintenance in living cells. J. Cell Biol. 180, 1101–1114.

Hollenbeck, P.J., 1993. Products of endocytosis and autophagy are retrieved from axons by regulated retrograde organelle transport. J. Cell Biol. 121, 305–315.

Hu, J., et al., 2009. A class of dynamin-like GTPases involved in the generation of the tubular ER network. Cell. 138, 549–561.

Huang, C.Y.M., Rasband, M.N., 2018. Axon initial segments: structure, function, and disease. Ann. N. Y. Acad. Sci. 1420, 46–61.

Hübner, C.A., Kurth, I., 2014. Membrane-shaping disorders: a common pathway in axon degeneration. Brain. 137, 3109–3121.

Jiang, M., Chen, G., 2006. High Ca2+−phosphate transfection efficiency in low-density neuronal cultures. Nat. Protoc. 1, 695–700.

Kim, Y.M., et al., 2015. mTORC1 phosphorylates UVRAG to negatively regulate autophagosome and endosome maturation. Mol. Cell 57, 207–218.

Kornak, U., et al., 2014. Sensory neuropathy with bone destruction due to a mutation in the membrane-shaping atlastin GTPase 3. Brain J. Neurol. 137, 683–692.

Krols, M., et al., 2018a. Sensory neuropathy-causing mutations in ATL3 affect ER-mitochondria contact sites and impair axonal mitochondrial distribution. Hum. Mol. Genet. 28, 615–627.

Krols, M., et al., 2018b. Sensory-neuropathy-causing mutations in ATL3 cause aberrant ER membrane tethering. Cell Rep. 23, 2026–2038.

Lee, S., et al., 2011. Lysosomal proteolysis inhibition selectively disrupts axonal transport of degradative organelles and causes an Alzheimer's-like axonal dystrophy. J. Neurosci. 31, 7817–7830.

Leterrier, C., 2018. The axon initial segment: an updated viewpoint. J. Neurosci. 38, 2135–2145.

Liang, J.R., et al., 2018. Atlastins remodel the endoplasmic reticulum for selective autophagy. J. Cell Biol. 217, 3354–3367.

Luarte, A., et al., 2018. The axonal endoplasmic reticulum: one organelle-many functions in development, maintenance, and plasticity. Dev. Neurobiol. 78, 181–208.

Maday, S., 2016. Mechanisms of neuronal homeostasis: autophagy in the axon. Brain Res. 1649, 143–150.

Maday, S., Holzbaur, E.L., 2012. Autophagosome assembly and cargo capture in the distal axon. Autophagy. 8, 858–860.

Maday, S., Holzbaur, E.L., 2014. Autophagosome biogenesis in primary neurons follows an ordered and spatially regulated pathway. Dev. Cell 30, 71–85.

Maday, S., Holzbaur, E.L., 2016. Compartment-specific regulation of autophagy in primary neurons. J. Neurosci. 36, 5933–5945.

Maday, S., et al., 2012a. Autophagosomes initiate distally and mature during transport toward the cell soma in primary neurons. J. Cell Biol. 196, 407–417.

Maday, S., et al., 2012b. Autophagosomes initiate distally and mature during transport toward the cell soma in primary neurons. J. Cell Biol. 196, 407–417.

McCorquodale 3rd, D.S., et al., 2011. Mutation screening of spastin, atlastin, and REEP1 in hereditary spastic paraplegia. Clin. Genet. 79, 523–530.

Mochida, K., et al., 2015. Receptor-mediated selective autophagy degrades the endoplasmic reticulum and the nucleus. Nature 522, 359.

Nakatogawa, H., 2020. Mechanisms governing autophagosome biogenesis. Nat. Rev. Mol. Cell Biol. 21, 439–458.

Nehls, S., et al., 2000. Dynamics and retention of misfolded proteins in native ER membranes. Nat. Cell Biol. 2, 288–295.

Niu, L.L., et al., 2019. Atlastin-mediated membrane tethering is critical for cargo mobility and exit from the endoplasmic reticulum. Proc. Natl. Acad. Sci. U. S. A. 116, 14029–14038.

Orso, G., et al., 2009. Homotypic fusion of ER membranes requires the dynamin-like GTPase atlastin. Nature. 460, 978–983.

Overhoff, M., et al., 2020. Mechanisms of neuronal survival safeguarded by endocytosis and autophagy. J. Neurochem. 157, 263–296.

Özkan, N., et al., 2020. ER – lysosome contacts at a pre-axonal region regulate axonal lysosome availability. bioRxiv. https://doi.org/10.1101/2020.06.16.153734, 2020.06.16.153734.

Ozturk, Z., et al., 2020. Axonal endoplasmic reticulum dynamics and its roles in neurodegeneration. Front. Neurosci. 14.

Pawar, S., et al., 2017. Efficient protein targeting to the inner nuclear membrane requires Atlastin-dependent maintenance of ER topology. Elife. 6.

Roussel, B.D., et al., 2013. Endoplasmic reticulum dysfunction in neurological disease. Lancet Neurol. 12, 105–118.

Sherer, N.M., et al., 2003. Visualization of retroviral replication in living cells reveals budding into multivesicular bodies. Traffic. 4, 785–801.

Shibata, Y., et al., 2006. Rough sheets and smooth tubules. Cell. 126, 435–439.

Shibata, Y., et al., 2008. The reticulon and DP1/Yop1p proteins form immobile oligomers in the tubular endoplasmic reticulum. J. Biol. Chem. 283, 18892–18904.

Stavoe, A.K.H., Holzbaur, E.L.F., 2019a. Autophagy in neurons. Annu. Rev. Cell Dev. Biol. 35, 477–500.

Stavoe, A.K.H., Holzbaur, E.L.F., 2019b. Axonal autophagy: mini-review for autophagy in the CNS. Neurosci. Lett. 697, 17–23.

Terasaki, M., 2018. Axonal endoplasmic reticulum is very narrow. J. Cell Sci. 131, jcs210450.

Timmerman, V., et al., 2013. Overlapping molecular pathological themes link Charcot-Marie-tooth neuropathies and hereditary spastic paraplegias. Exp. Neurol. 246, 14–25.

Wacker, I., et al., 1997. Microtubule-dependent transport of secretory vesicles visualized in real time with a GFP-tagged secretory protein. J. Cell Sci. 110, 1453–1463.

Wang, T., et al., 2015. Control of autophagosome axonal retrograde flux by presynaptic activity unveiled using botulinum neurotoxin type a. J. Neurosci. 35, 6179–6194.

Wang, Y., et al., 2018. Neuronal autophagy and axon degeneration. Cell. Mol. Life Sci. 75, 2389–2406.

Westrate, L.M., et al., 2015. Form follows function: the importance of endoplasmic reticulum shape. Annu. Rev. Biochem. 84, 791–811.

Wilkinson, S., 2019. ER-phagy: shaping up and destressing the endoplasmic reticulum. FEBS J. 286, 2645–2663.

Wu, Y.M., et al., 2017. Contacts between the endoplasmic reticulum and other membranes in neurons. Proc. Natl. Acad. Sci. U. S. A. 114, E4859–E4867.

Yalcin, B., et al., 2017. Modeling of axonal endoplasmic reticulum network by spastic paraplegia proteins. Elife. 6.

Yamanaka, T., Nukina, N., 2018. ER dynamics and derangement in neurological diseases. Front. Neurosci. 12.